Journal of Electric Propulsion

RESEARCH Open Access

Numerical framework for the development of atmosphere-breathing electric propulsion for Earth and Mars atmosphere

Valentina Pessina[1*], Maria Smirnova[2] and Jochen Schein[1]

*Correspondence:
valentina.pessina@unibw.de

[1] Institute of Physics, University of the Bundeswehr Munich, Werner-Heisenberg-Weg 39, Neubiberg, Munich 85577, Germany
[2] TransMIT GmbH, Gießen 35390, Germany

Abstract

Atmosphere-breathing electric propulsion systems provide a competitive advantage for the lower orbit altitudes since the propellant is collected directly from the atmosphere. The effectiveness of this technology depends on crucial aspects such as the collection and compression performance characterization, as well as the drag estimation and compensation. In the first part of this study, the lower Mars and Earth atmospheric characterization is derived based on current models and mission data. This characterization is a reliable dataset for the boundary conditions for the simulations carried out in the second part of this study. The proposed computational framework based on the Direct Simulation Monte Carlo method aims to investigate the collection and compression performances and to estimate the drag. The numerical comparison with a literature case validates the numerical setup presented in this study. The effect of different gas-surface interaction models is investigated by comparing the results yielded by the Maxwellian model (fully specular and partially diffuse reflection) and the Cercignani-Lampis-Lord model. Since the intermolecular collisions can become more relevant at the inlet of the ionization stage, both the variable hard and variable soft sphere models are briefly examined, as well as the inclusion of gas-phase reactions. Finally, the simulation results of the two cases for the low Mars orbit (150 and 140 km) are compared to the Earth case (180 km).

Keywords: Atomosphre-breathing electric propulsion, Low Earth orbit, Direct simulation Monte Carlo, Mars, Earth

Introduction

The main innovative idea behind Atmosphere Breathing Electric Propulsion (ABEP) systems is that the propellant is collected directly from the atmosphere. An intrinsic advantage of this technology is that an onboard fuel tank is not strictly required. Hence, if coupled with a plasma generation source with a reduced tendency to erosion and wear, the lifetime of the satellite mission powered by ABEP can be extended. Several concepts were presented as reported in numerous recent review studies [1–3] and recent works [4, 5], both targeting Low Earth Orbits (LEO) and Very Low Earth Orbits (VLEO) with projects such as the RAM-EP [5] by the European Space Agency (ESA), the studies in collaboration with Japan Aerospace Exploration Agency (JAXA) [6, 7], the Air-breathing

Electric THrustER (AETHER) [8] project, or the different designs proposed by universities [9–11], and additionally the proposal for Mars in the Martian Atmosphere Breathing Hall Effect Thruster (MABHET) [4]. Generally, the ABEP systems target lower orbits, where the atmosphere is dense enough to provide an adequate mass flow rate, which is determined by the thrust required to prevent unplanned deorbiting. The low-orbit target is an additional advantage in terms of launch costs [12]. However, at lower orbits, the increased aerodynamic drag experienced by the spacecraft (S/C) demands a thrust capable of full compensation, hence the effective collection of atmospheric particles. From the schematics shown in Fig. 1, one can split the design of ABEP into three main strategic steps: the characterization of the *fuelling propellant*, hence the knowledge of the available atmospheric gas, the design of an effective intake-compression-thermalization stage, which should be designed based on the *rarefied gas-dynamics*, and finally an efficient *electric thruster* where the gas is ionized and accelerated based on the selected propulsion system principles. Although these three aspects are inherently connected, this paper focuses on the first two, aiming to provide a numerical framework for the intake design for the atmosphere of both Earth and Mars. The use of the rarefied gas-dynamics [13] and the Direct Simulation Monte Carlo (DSMC) method [14] is the essential base employed in this study to tackle the design of ABEP systems since it can provide an estimation of the drag to be compensated by the thrust, as well as information regarding the intake design. The DSMC simulation has proven to be an effective tool for intake design purposes, as shown in several Earth-related studies targeting VLEO applications, such as the comparison of different intake designs [11] targeting the low orbital altitudes for Earth from 150 km to 250 km with PIC-DMSC-code PICLas [15], or the comparison of different inlet duct patterns with the help of dsmcFoam+ [16], or the inlet flow simulations of ABEP systems with Stochastic PArallel Rarefied-gas Time-accurate Analyzer (SPARTA) DSMC-solver [17–19]. These studies offer a detailed methodology for the geometric intake design for Earth applications, with more or less complex gas-surface interaction (GSI) description, whereas DSMC simulations for Martian applications are rare in the literature. This study aims to apply the DSMC-based simulations for the ABEP system development with the actual conditions experienced by the orbiting satellite to estimate the key parameters for the ABEP design, such as the compression performances, the mass flux to the thruster, and a final remark on the aerodynamic drag D.

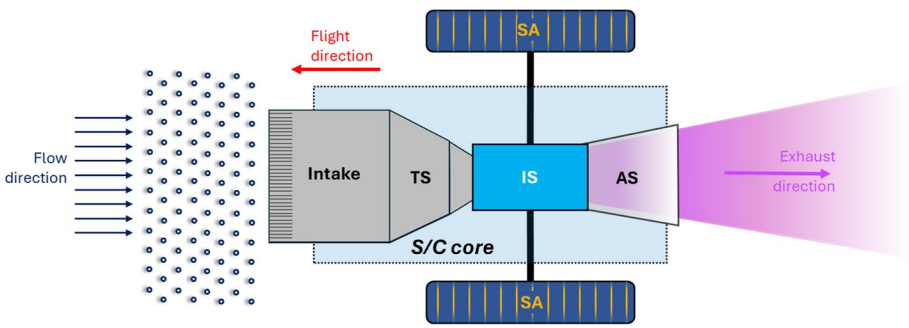

Fig. 1 Schematics of ABEP system: intake, thermalization stage (TS), ionization stage (IS), acceleration stage (AS), solar array (SA), and spacecraft (S/C) core

After providing the atmospheric characterization for Earth 120 km to 260 km) and Mars (100 km to 200 km), the numerical framework is applied to a VLEO case at 180 km and to low Mars orbit of 140 km and 150 km altitude. For a simplified geometry from literature [18], the impact of the GSI modelling is investigated for the Earth case by comparing simulation results from specular to partial and total diffuse reflection based on the Maxwellian model [20], as well as the Cercignani-Lampis-Lord model [21, 22], which assumes that the reflected particles have a lobular distribution. A brief check on the impact of the intermolecular collision model is carried out with variable hard sphere (VHS) and with variable soft sphere (VSS) since after the compression, the mean free path between the particles decreases compared to the one from the free molecular flow around the S/C. Finally, the application to the atmosphere of Mars is presented with a comparison drawn for the collection and compression performances, as well as for the drag.

Methodology

Atmospheric characterization

The aim of the atmospheric characterization consists of the description of the variation with the altitude of the gas properties such as density and temperature, as well as the composition, which are the boundary conditions for the ABEP system simulations and operation. In this study, the characterization focuses on a wide low-altitude range for both Earth, (120 km to 260 km) and Mars (100 km to 200 km). First, the published information is gathered from previous missions and atmospheric models, and then the values of temperature, density, and composition are interpolated to build a database with a 10 km step size. This way, the values can be compared for a given altitude thanks to the customized altitude step size obtained with the interpolation. The reference for Earth atmospheric characterization is the NRLMSISE-00 model [23, 24]. The NRLMSIS 2.0 model [25] is the updated and more recent version of the NRLMSISE-00 with enhanced solar activity characterization, improved minor species and density prediction. The NRLMSIS 2.0 is adopted for advanced space science and engineering applications, whereas this study aims at using the NRLMSISE-00 to provide average representative values for the altitudes of interest, without considering the variations due to the solar activity and the geolocation. As for the Martian atmosphere, the data from several missions are compared. The temperature is extracted from the data provided by the Viking 1 and 2 landers [26, 27]. The characterization of the mass density variation with the altitude is crucial for determining the performance of the ABEP systems for a given orbit altitude, since the density directly impacts both the aerodynamic drag force experienced by the satellite $\left({}^{D}/_{A_{ref}} \propto \rho c_d v_{orb.}^2\right)$ and the mass flow rate to the ionization and acceleration stage, hence the obtainable thrust. The density data from different Mars missions are compared to the one of the NRLMSISE-00 for the Earth in Fig. 2: the fitting function proposed by Blanchard based on the reentry measurements of Viking 1 lander [28], the data from Mars-GRAM 2000 [29], and the Pathfinder [30]. The density from the data from the Martian atmosphere and Volatile EvolutioN (MAVEN) and Mariner 9 is derived in this study based on the ideal gas law and the total number density. As a first approximation of the total number density, the charged particles are neglected in the

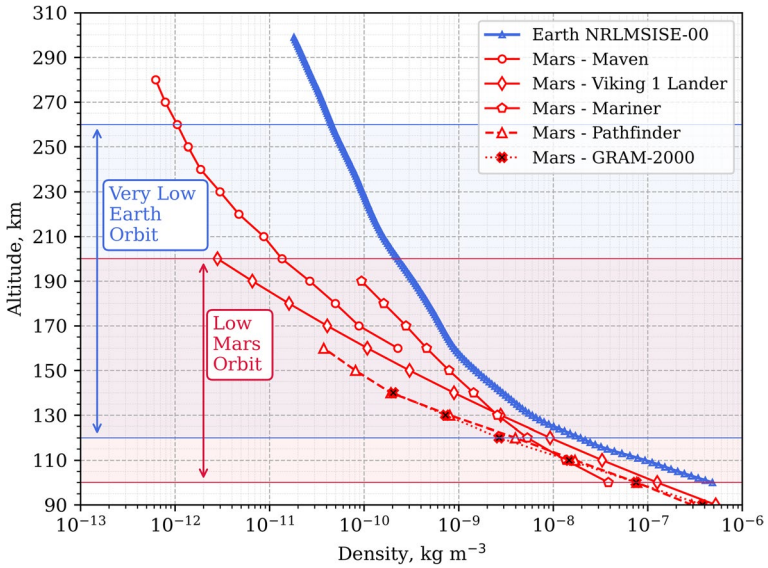

Fig. 2 Density with altitudes: data from NRLMSISE-00 for Earth, for Mars the comparison between different missions

sum since they have a negligible number density ranging from 10^6 to 10^{11} m^{-3} compared to the neutrals, which ranges between 10^{14} to 10^{18} m^{-3} (example at 100 km).

From the total number density n_{tot}, the mole fraction x_i of each species i, the average molecular weight is estimated based on a mole-based average, and finally, the mass density of the atmospheric gas is derived based on the ideal gas assumption as per Eq. (1):

$$\rho = {}^{(n_{tot} MW_{ave})}/_{\mathrm{N_A}} \tag{1}$$

The temperature and density of Earth and Mars for low orbits are compared in Fig. 3, whereas the density comparison between the analyzed Martian missions is summarized in Fig. 2. As for the atmospheric composition, the ultraviolet spectrometer observations, airglow measurements from Mariner 9 mission (100 km to 200 km) are collected [31, 32] as the initial set of data.

A second dataset is derived from the measurements during the descent of the Viking 1 lander (1976), which was equipped with the Upper Atmosphere Mass Spectrometer (UAMS) and a Retarding Potential Analyzer (RPA) [33]. The third dataset for the composition is taken from the more recent observations by MAVEN from 155 km to 200 km [34] and for lower altitudes [35]. The reference composition of the main 9 species (CO_2, CO, NO, N, N_2, O_2, O, Ar, He) is derived from the more recent observations by MAVEN as shown in Fig. 4b. As for Earth, the NRLMSISE-00 model is consistently taken as a reference, and the neutral number density values for the main 7 species (N_2, N, O_2, O, Ar, He, H) is drawn in Fig. 4a.

Direct Simulation Monte Carlo Method and simulation setup

The DSMC method [14] provides a stochastic description of a representative population of particles based on the Boltzmann equation for the gas kinetics. For each particle, the instantaneous values of the properties of interest are then averaged to obtain a statistically

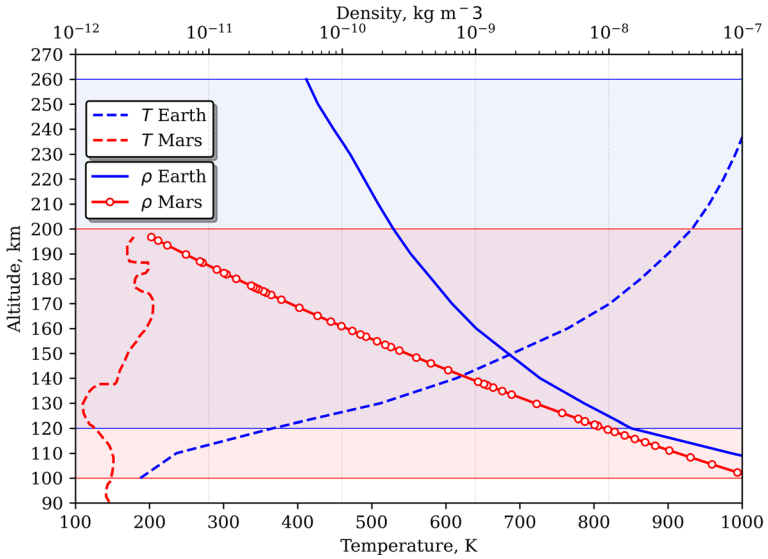

Fig. 3 Variation of temperature and density with the altitude. The altitude range of interest is highlighted in red for Mars, in blue for Earth

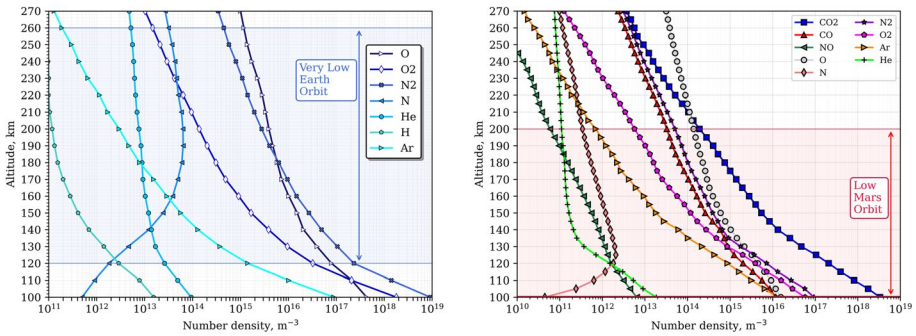

Fig. 4 Earth atmospheric composition from NRLMSISE-00 (**a**). Mars atmospheric composition: data from NGISM-MAVEN (**b**)

relevant description. Finally, the macroscopic fluid properties can be estimated as the average of the values assumed by the set of particles belonging to a given computational cell. The DSMC method is suitable for rarefied gas dynamics problems since it is effective for both the transitional flow regime ($0.1 \leq Kn \leq 10$) and the free molecular flow regime ($Kn > 10$). The flow regime can be identified based on the Knudsen number (Kn), which is generally defined as the ratio of the molecular mean free path λ and the characteristic length of the problem L_c. For the free-stream, the value of λ in Eq. (3) varies with the altitude (Fig. 5), as both n_{tot} and the reference diameter d_{ref}, which is calculated as the averaged reference diameter of each species i weighted with the mole fraction x_i as per Eq. (2), hence based on the composition analogously to the MW_{ave}.

$$d_{ref} = \sum_i x_i \cdot d_{ref,i} \tag{2}$$

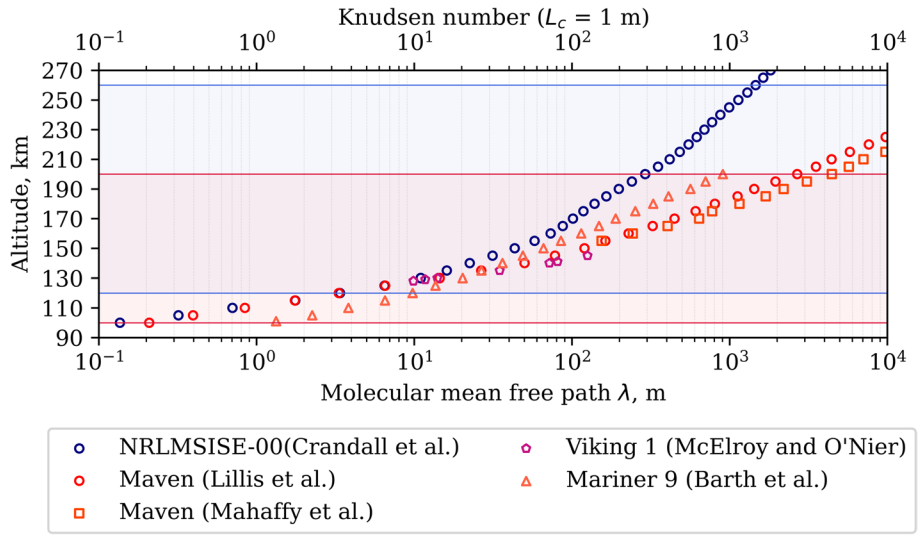

Fig. 5 Free-stream conditions: variation with the altitude of the molecular mean free path (λ) and Knudsen number (Kn) in case of characteristic length L_c of 1 m

$$\lambda = \frac{k_B \cdot N_A}{\sqrt{2} \cdot \pi \cdot R} \cdot \frac{1}{d_{ref}^2 \cdot n_{tot}} \tag{3}$$

As the definition suggests, the Kn also varies with the selected L_c, which can be set equal to the intake inlet diameter (e.g. ~1.5m [18]) or the ionization stage inlet diameter (e.g. ~0.08 m [18]), hence λ is preferred for the grid size definition. Once the altitude of interest for a DSMC simulation is selected, λ is uniquely determined by n_{tot} and the averaged d_{ref}, and from this information the computational grid dimension L_{cell} can be set accordingly to this constrain: ${}^{L_{cell}}/_{\lambda} \ll 1$. In the same fashion of λ and Kn, the speed ratio s Eq. (4) can shed light on the more relevant collision phenomena.

$$s = \frac{v_b}{v_{thermal}} = \frac{v_b}{\sqrt{\left(\frac{2 \cdot T \cdot k_B}{m_p}\right)}} \tag{4}$$

In the case of hyperthermal flows ($s > 5$), the Brownian motions are less relevant than the surface-particle collisions, making the GSI modelling a priority over the intermolecular collision model, and vice versa for thermal flow (s ~1), where the random molecular motion becomes more relevant than the collective motion. In the case of ABEP, the free-stream flow is in hyperthermal conditions, and then the particles start to collide with the surface, partially being reflected, partially being collected in the intake, where the Brownian motions and random collisions result in a thermalization of the flow, which slows down, thus providing a compression effect. In light of these observations, both GSI and interparticle collisions are relevant, and their accurate modelling is necessary. The interparticle collisions and the anisotropic scattering is described with both the Variable Hard Sphere (VHS) and the Variable Soft Sphere (VSS). The input parameters for the VHS model shown in Table 1 are derived from

[14, 36], whereas the VSS parameters are suggested by the recent work by Pfeiffer [37].

As with interparticle collisions, the particle-surface collision description is analogously important. In this study, the results yielded by different models are compared based on the compression effect due to thermalization. After the intake, the collected particles slow down as a consequence of the repeated collisions with the surrounding surfaces, hence the collected rarefied gas is thermalized and subject to compression. The most popular GSI model for the calculation of post-collision kinetic energy is the partially diffuse reflection by Maxwell [14, 20], in which only a fraction of the impinging particles are specularly reflected, while the remaining are fully accommodated (complete diffuse reflection), depending on the value of the accommodation factor α_{acc} described in Eq. (5).

$$\alpha_{acc} = \frac{E_i - E_r}{E_i - E_w} \tag{5}$$

The accommodation coefficient can vary between one and zero. The zero value indicates the fully specular reflection in which the pre- and post-collision kinetic energy of the particle is unchanged after the specular reflection. In case of α_{acc} equal to unity, the fully diffuse reflection occurs, and the post-collision particle is in thermal equilibrium with the wall. However, as demonstrated by Cercignani and Lampis [21], a more realistic reflection pattern for a molecular beam is described by a lobular distribution in the direction of the re-emitted particle velocity vectors. Unlike the Maxwellian model, two post-collision characteristic temperatures of the reflected particles are defined: one for the scattering kernel of the tangential velocity, and one for the kernel of the normal velocity. The modification of this model done by Lord includes the diffuse scattering with partial energy accommodation, and also the vibrational accommodation [22]. The Cercignani-Lampis-Lord (CLL) [21, 22] model as implemented in the SPARTA DSMC solver [36] allows the use of different accommodation coefficients: a coefficient for the accommodation in the tangential direction and one for the normal direction ($\alpha_{acc,t}$ and $\alpha_{acc,n}$), then one for the vibrational and rotational energy accommodation ($\alpha_{acc,vib}$ and $\alpha_{acc,rot}$ respectively). In this study, the results yielded by the GSI modelling with specular, diffuse, and partially diffuse scattering with the Maxwellian model is compared with the

Table 1 VSS and VHS parameters for modelling the interparticle collisions

		VHS			VSS		
Species	**mass (kg)**	**ω (-)**	**d_{ref} (m)**	**α (-)**	**ω (-)**	**d_{ref} (m)**	**α (-)**
O_2	5.310×10^{-26}	0.77	3.96×10^{-10}	1.00	0.702	3.773×10^{-10}	1.391
N_2	4.650×10^{-26}	0.74	4.07×10^{-10}	1.00	0.693	3.911×10^{-10}	1.351
O	2.650×10^{-26}	0.80	3.00×10^{-10}	1.00	0.772	3.340×10^{-10}	1.471
N	2.325×10^{-26}	0.80	3.00×10^{-10}	1.00	0.753	3.402×10^{-10}	1.477
NO	4.980×10^{-26}	0.79	4.20×10^{-10}	1.00	0.716	3.983×10^{-10}	1.425
CO_2	7.310×10^{-26}	0.93	5.62×10^{-10}	1.00	0.693	4.647×10^{-10}	1.37
CO	4.650×10^{-26}	0.73	4.19×10^{-10}	1.00	0.726	4.101×10^{-10}	1.34
Ar	6.630×10^{-26}	0.81	4.17×10^{-10}	1.00	0.700	3.832×10^{-10}	1.384

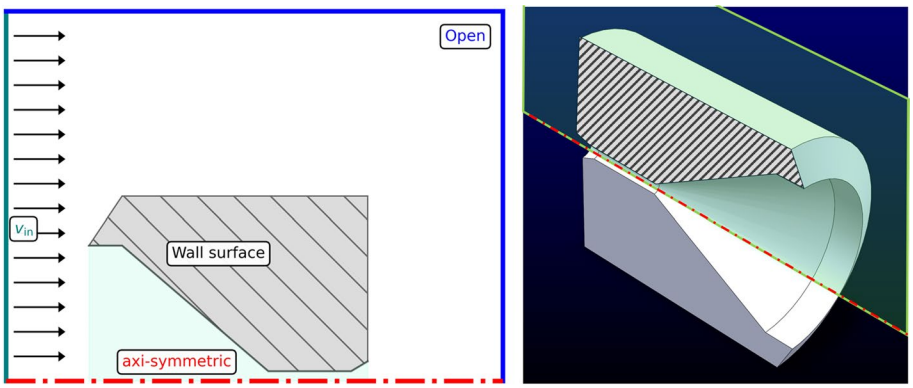

Fig. 6 Computational domain schematics (**a**) with boundary conditions highlighted, and a 3D schematics of the simplified geometry

Table 2 Comparison between the grid cell size and the molecular mean free path for 180 km altitude of the Earth atmosphere

Refinement Lev. →	Level 1	Level 2	Level 3	Level 4
L_{cell} →	0.1 m	0.05 m	0.025 m	0.0125 m

results yielded by the CLL GSI model. Finally, for the test case in the atmosphere of the Earth, the role of the reactions within the neutral gas phase is investigated. For the Total Collision Energy (TCE), a reaction list for the Earth's species is set based on the results reported by the NASA study [38]. The DSMC simulations aim to investigate and characterize the flow parameters of the intake of a simplified geometry, such as mass and number density, and pressure, and eventual indications of the intake capabilities.

Computational domain and grid

The simplified slope geometry proposed by Jin et al. [18] is shown in a 3D cut section in Fig. 6b, along with the schematization of the boundary conditions assigned to the computational domain in Fig. 6a. The 1D axisymmetric computational domain comprises an axisymmetric boundary and an open boundary around the far field, with one of them set as an equivalent in-flow boundary on which the number of particles and their velocity are set. The ABEP surface is set as a wall boundary with a GSI model.

The total extension of the domain is at least 6 times bigger than the total length of the ABEP (L=1.7 m) along the axisymmetry axis direction, and at more than four times the max external radius of the ABEP (~0.75m). The cartesian grid created for this study is the same for the Mars and Earth test cases, since its grid dimension satisfies the condition of $^{L_{\text{cell}}}/_{\lambda} \ll 1$ for both cases. More specifically, the estimation of L_{cell} is done based on the estimated d_{ref} at 180 km of the atmosphere of Earth, and the average values of the local number density extracted from a first round of simulations serving the purpose of gird size definition before the final round of cases. A summary of the different values of L_{cell} for each level of the refinement is provided in Table 2. Besides the multi-level static refinement, for each case, an adaptive refinement and coarsening is carried out

to optimize the computational cost. The grid adaptation criterion is based on lower and higher thresholds for the local value of n_{tot}, which is linked to λ in virtu of Eq. (3), and the final result is shown in Fig. 7. The simulation box size is 12 m along the axisymmetric axis (y axis), and 4 m in the orthogonal direction (x axis). The simulation timestep is set to 1×10^{-6} s, and the total number of simulated particles is adjusted to have at least 20 particles per cell, even in the refined areas. For the Earth cases, the timestep choice should be 5e-7 s for a minimum cell size of 12.5 mm and a maximum velocity of 7760 m/s. However, in the mesh refinement inside the intake with the minimum cell size, the maximum velocity values are below 3000 m/s, hence the portion of the cell crossed per timestep is less than 30%, whereas in the outer part, the maximum particle velocity in the refined area close to the outer intake surface is below 4000-4500 m/s. Hence the $\sim$ 32%-36% of the cell length is crossed by the particles per timestep. Thus, to contain the computational cost, the cell length traveled by the particles per timestep is kept around one third of the total length.

The reason behind the selection of this test-geometry from literature [18] is twofold: first, a simple geometry is easier to handle for the numerical-to-numerical validation between the results discussed by Jin et al. [18] and the ones from this study, and second, the simplified geometry is a starting point to isolate the impact of the models on the estimation of the quantities of interest. However, whereas the the analysis presented by Jin et al. [18] focuses on the inlet geometries with a Maxwellian GSI model, this study aims to investigate the different results yielded by different GSI models for a given geometry, adding the comparison with the CLL GSI model, to explore the eventual differences yielded by VHS and VSS, and finally, to apply it to the case of the Martian atmosphere.

Results and discussion

The results for the simplified test geometry are reported in this section, starting with a numerical validation with the reference case from literature [18]. Once the numerical setup (grid and models) are at least numerically validated, the compression and collection performances yielded by different GSI models are analyzed for the reference case for 180 km altitude of Earth's atmosphere. Although less relevant if compared to the GSI model, the interparticle collision model VHS and VSS are also compared, and additionally, the impact of the gas-phase reactions is tested. Then, the application of this simple slope geometry is extended to the Martian atmosphere examining two different

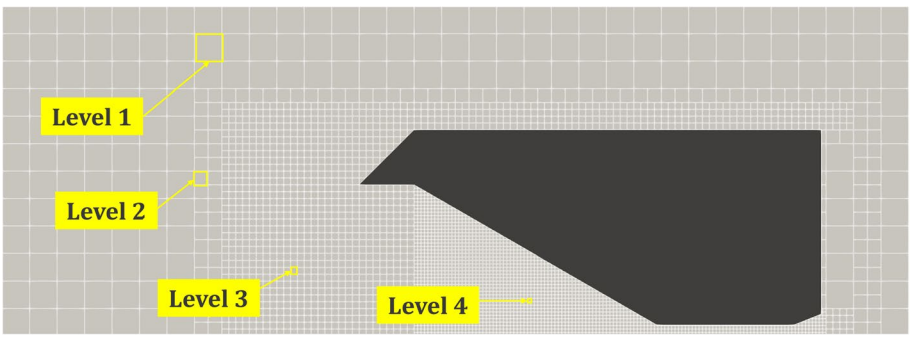

Fig. 7 Grid detail: multi-level refinement of the cartesian grid, after the grid adaptation

Table 3 Boundary conditions for the Earth atmosphere cases corresponding to the free-stream conditions at 180 km altitude

h (km)	ρ_∞ (kg m^{-3})	n_{tot} (m^{-3})	T_∞ (K)	p_∞ (Pa)	v_∞ (m s^{-1})	x_O (-)	x_{N_2} (-)	x_{O_2} (-)
180	5.198×10^{-10}	1.4×10^{16}	790	1.523×10^{-4}	7760	0.4820	0.4829	0.0351

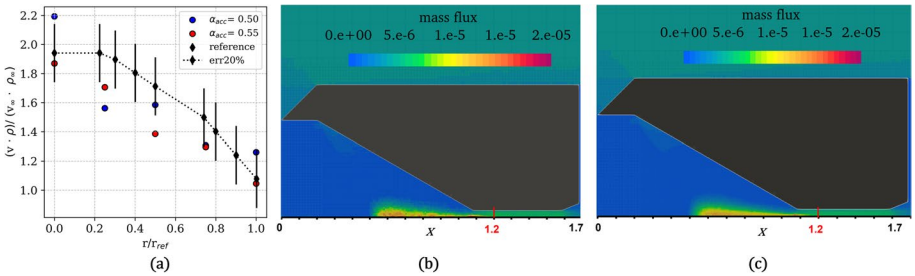

Fig. 8 Result of mass flux (kg · m^{-2} · s^{-1}) evaluated at 1.2 m (section in red): values compared to the reference case (**a**) and contour plots for Maxwellian model with α_{acc} set to 0.5 (**b**) and 0.55 (**c**)

altitudes, 150 and 140 km, which are chosen to match respectively the free-stream gas density (ρ_∞) and theoretical intake mass-flux ($v_\infty \cdot \rho_\infty$) of the 180 km Earth case.

Numerical setup validation

The numerical setup quality is assessed by the comparison with the reference case from literature [18], for the slope geometry and boundary conditions relating to a VLEO orbit altitude of 180 km as summarized in Table 3.

The GSI model for the validation is the Maxwellian model with a partially diffuse reflection ($\alpha_{acc} = 0.5$). The intermolecular collisions are described with the VHS model, and the gas-phase reactions are neglected. The alignment between this study results and the reference case is achieved with a satisfactory agreement in terms of pressure values along the axisymmetry axis and the gas mass flux through the selected cross-section at the entrance of the ionization stage, which is located 1.2 m from the intake inlet section. The values of the mass flux ($v \cdot \rho$) are reported in Fig. 8a: the error is within 20% maximum for the majority of the points corresponding to the values in the radial direction of the cross-section defined at 1.2 m of axial length (highlighted in red in Fig. 8b); the contour plots are representative of the mass flux (kg · m^{-2} · s^{-1}) for the reference value of the accommodation coefficient (α_{acc}=0.5) in Fig. 8b and for an increase in its value of 10% (α_{acc}=0.55) in Fig. 8c. The value of the pressure along the axisymmetry axis is shown in Fig. 9a along with the case of α_{acc}=0.55 in Fig. 9b, as well as the number density in Fig. 9c, and the maximum error is below 2%, and below 5% for the case α_{acc}=0.5.

The mass flux measured on the ionization stage inlet on the center line can be considered as the key information from the DSMC for drawing conclusions on the collection performance, hence the values obtained for the α_{acc} set as 0.55 are in agreement with the reference study. However, for the points between the wall and the centerline laying on the considered cross section, the agreement is less satisfying. If the values across the whole section are of relevance, further investigation should be carried out with additional studies that include both the velocity and the density to isolate the source of the

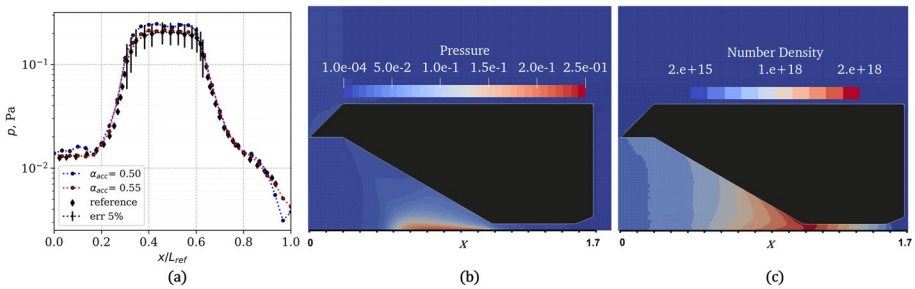

Fig. 9 Result of pressure along the axi-symmetry axis direction (**a**) and contour plot of the pressure in Pa (**b**) and number density in m^{-3} (**c**) for $\alpha_{acc} = 0.55$

Table 4 Case setup summary for Earth atmosphere: the setup variations including the intermolecular collision, gas-surface interaction, and gas-phase reactions

Case ID	Case 1	Case 2	Case 3	Case 4	Case 5	Case 6	Case 7
GSI model	Maxwell	Maxwell	Maxwell	Maxwell	Specular	CLL	CLL
α_{acc} (for Maxw.)	0.55	0.55	0.55	1.0	0.0		
α_n (for CLL)						0.55	0.55
α_t (for CLL)						0.55	0.75
Intermolecular collisions	VHS	VHS	VSS	VHS	VHS	VHS	VHS
Gas-phase reactions	none	TCE	none	none	none	none	none

error. Since the pressure error along the whole center line is under 5% for the α_{acc} set to 0.5 and under 2% for the α_{acc} set to 0.55, and since the mass flux matches partially (near the wall and along the center line) the reference case, the validation can be completed. An additional validation for the drag force is carried out in the corresponding section.

Performances in Earth atmosphere

The DSMC simulation results are discussed in terms of collection and compression performances of the simplified geometry for 180 km altitude in Earth's atmosphere. The aim is to highlight the different results yielded by the GSI model (Specular, Maxwellian, and CLL) first, as well as the intermolecular collision models (VHS and VSS), which become more relevant between the thermalization and ionization stage due to the increased number density, generally two orders of magnitudes higher than the free stream. The 2D axisymmetric simulations are carried out with the boundary conditions summarized in Table 3, and each case is run with a specific setup to isolate the variation of collection and compression performances due to either the intermolecular collision, GSI, or gas-phase chemistry model.

The simulation setup variation for each case is listed in Table 4, with a composition based on the predominant species at 180 km altitude (O, O_2, N_2) from Table 3. The compression performance can be evaluated by the pressure values along the axisymmetry line (Fig. 10). The total length L of the ABEP along the axial direction is 1.7 m, and after 0.4 m from the intake inlet section (located at $x = 0$ m), the compression effect can be observed. The pressure increase is visible until the ionization section ($\sim 1 \div 1.2$ m), after which the pressure starts dropping. Compared to the free-stream

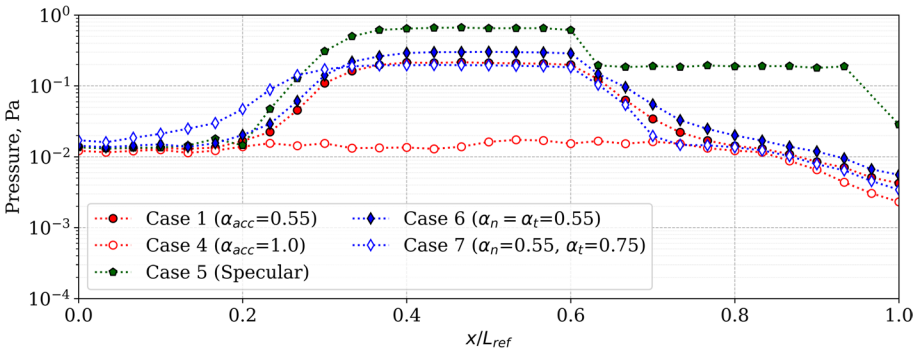

Fig. 10 Values of the pressure along the center line for each case relating to Earth (Table 4). The total length L_{ref} is 1.7 m

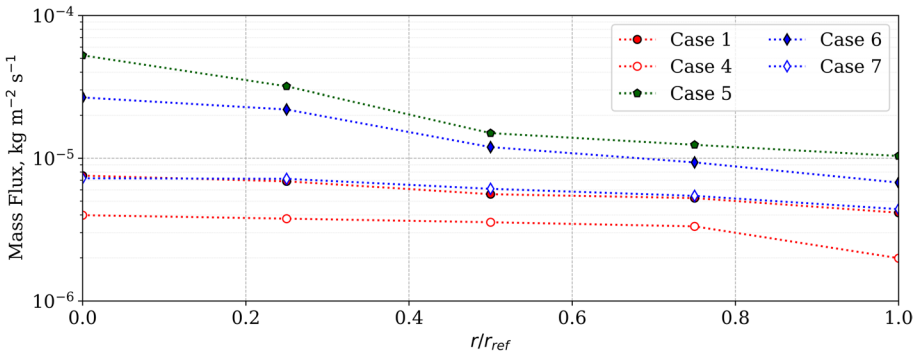

Fig. 11 Mass flux values on the cross section of the ionization stage (r_{ref} = 0.04m) at 1.2 m from the intake inlet. For all cases, the intermolecular collision is modelled with the VHS, whereas the GSI varies from the Maxwellian model (red), specular (green), and lobular CLL (blue)

pressure value of approximately 1.523×10^{-4} Pa, the compression effect results in a pressure increase of up to 0.2 Pa for the Maxwellian partially diffuse reflection (α_{acc}), as well as for the lobular reflection with anisotropic scattering ($\alpha_n = 0.55$ and $\alpha_t = 0.75$), and slightly higher for lobular reflection with isotropic scattering. From the intake inlet to the first part of the thermalization stage, case 1 and case 6 (all accommodation coefficients set to 0.55) yields similar pressure values, as expected, whereas from the thermalization to the outlet of the ABEP intake, case 1, 6, and 7 result in similar pressure values as shown in Fig. 10. As for the mass flux, it is unexpected that case 7 is closer to case 1 than case 6 (Fig. 11). The mass flux mismatch between case 1 and case 6, respectively with the Maxwellian model and $\alpha_{acc} = 0.55$ and the CLL model with $\alpha_n = \alpha_t = 0.55$, might be a result of the mass flux fluctuations in the section measured at 1.2 m along the center line, as seen in Fig. 8 in the validation section.

As for the interparticle collision models, the VHS and VSS models yield similar results for the examined altitude. The limited differences in Fig. 12 are reported for the compression performance (Fig. 12a), the mass flux (Fig. 12b) as well as the number density contour plot (Fig. 12c). A similar trend is expected in case of DSMC simulation modelled as free-molecular flow, hence with no interparticle collisions.

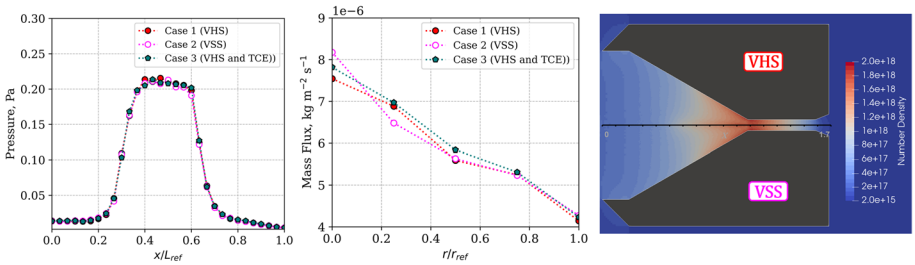

(a) (b) (c)

Fig. 12 Results from VHS and VSS intermolecular collision models, and TCE for VHS. Pressure (a) and mass flux (b) with a linear scale; number density contour plot (c) for VHS (top) and VSS (bottom)

Table 5 Composition of the free-stream set as boundary conditions for each simulation for Martian atmosphere

Case ID	h (km)	x_{CO_2} (-)	x_O (-)	x_{N_2} (-)	x_{C_O} (-)	x_{Ar} (-)	x_{O_2} (-)
Case 1 (Earth)	180	-	0.4820	0.4829	-	-	0.0351
Case 8 (Mars)	140	0.8365	0.0650	0.0415	0.0360	0.0039	0.0171
Case 9 (Mars)	150	0.7984	0.0870	0.0570	0.0380	0.0026	0.0170

Performances in Mars atmosphere

The Martian atmosphere investigation targets two different altitudes, 140 km and 150 km, with the VHS model for interparticle collisions and a partially diffuse reflection with the Maxwellian model (α_{acc}=0.55) for the particle-surface collisions. The investigated altitudes are selected to match either the gas mass density of the VLEO at 180 km altitude (150 km), or the product of the mass density and the orbiting velocity, hence to match the theoretical mass flux at intake inlet ($\rho_\infty \cdot v_\infty$). In this case study, the ABEP orbital velocity is 3400 m s^{-1}, which is ~44% less than the average orbiting velocity selected for the VLEO simulations. The results are a theoretical intake inlet mass flux of $\sim 3.75 \times 10^{-6}$ kg m^{-2} s^{-1} for Mars at 140 km altitude and $\sim 1.53 \times 10^{-6}$ kg m^{-2} s^{-1} at 150 km, compared to $\sim 4.03 \times 10^{-6}$ kg m^{-2} s^{-1} of the VLEO case at 180 km. The boundary conditions are extracted from the atmospheric characterization previously discussed, and the reference mission for density and composition is the MAVEN [34, 35] mission. For each altitude, the free-stream composition is set as the six most relevant species, characterized by the higher volume fraction, as summarized in Table 5. The temperature reference for the free-stream is deducted from the Viking 1 lander measurements, and consequently, the wall temperature is adjusted to a value closer to the free-stream conditions, thus set to 150 K. The boundary conditions for the two Mars cases are summarized in Table 6. For this comparison between Earth and Mars, the selected GSI model is the Maxwellian with partially diffuse reflection ($\alpha_{acc} = 0.55$), VHS model for the intermolecular collisions, with no gas-phase reactions. The number density contour plot in Fig. 13 of case 1 (Earth, 180 km) appears very similar to the one from case 8 (Mars, 140 km).

The compression performance is reduced for the Mars cases: the pressure along the stagnation line is 50% less for case 8 and 80% less for case 9 if compared to case 1 from Earth as shown in Fig. 14a. However, the design of the intake and collection stage is not optimized

Table 6 Boundary conditions for the Mars atmosphere cases corresponding to the free-stream conditions

Case ID	h (km)	ρ_∞ (kg m^{-3})	n_{tot} (m^{-3})	T_∞ (K)	p_∞ (Pa)	v_∞ (m s^{-1})	$\rho_\infty \cdot v_\infty$ kg m^{-2} s^{-1}
Case 1 (Earth)	180	5.2×10^{-10}	1.4×10^{16}	790	1.5×10^{-4}	7760	$\sim 4.03 \times 10^{-6}$
Case 8 (Mars)	140	1.1×10^{-9}	1.6×10^{16}	158	3.5×10^{-5}	3400	$\sim 3.75 \times 10^{-6}$
Case 9 (Mars)	150	4.5×10^{-10}	6.8×10^{15}	171	1.6×10^{-5}	3400	$\sim 1.53 \times 10^{-6}$

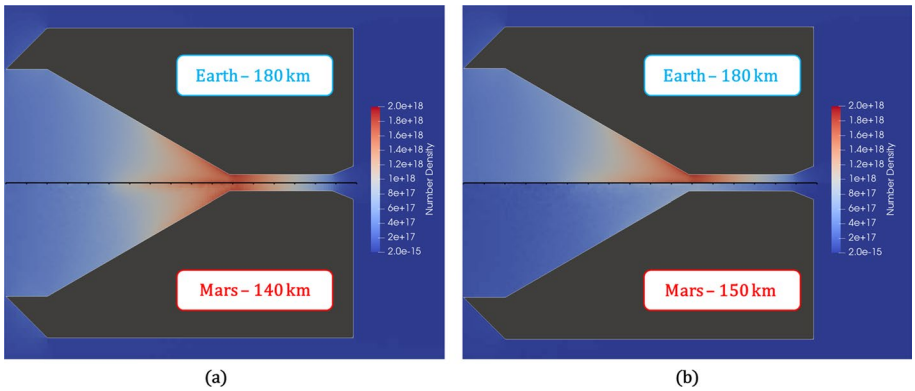

Fig. 13 Contour plots of number density values for Martian atmosphere at 140 km (**a**) and 150 km (**b**) compared to Earth at 180 km. The reference conditions are reported in Tables 5 and 6

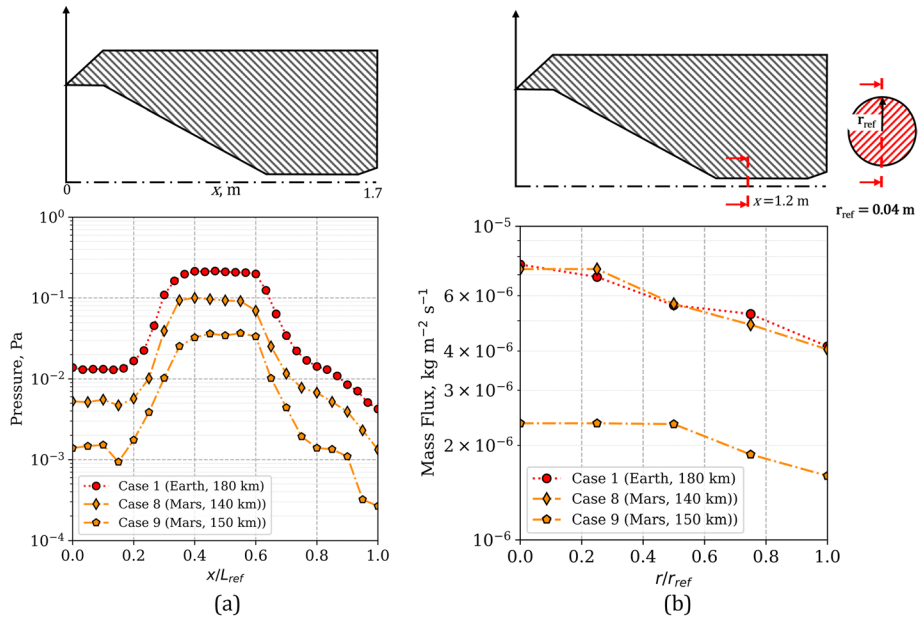

Fig. 14 Pressure along the axi-symmetry axis (**a**), mass flux at the cross-section of the ionization stage inlet (**b**)

nor designed specifically for Mars applications, hence the addition of a molecular trap at the intake inlet, along with the design optimization might improve the compression performance. An analogous outcome is observed for the mass flux in Fig. 14b, suggesting a design improvement.

Drag force: Mars and Earth

One of the vital aspects of the ABEP design is the capacity to compensate fully the drag force. The theory behind the aerodynamic drag force for satellite applications has been extensively studied in literature [39, 40], and in this study the aim is to provide a general estimation of the drag force from the DSMC simulations for the simple slope geometry for Mars (140 km) and Earth (180 km). The aerodynamic drag force D is defined as in Eq. (6):

$$D = \frac{1}{2} c_d A_{ref} \rho v^2 \tag{6}$$

where A_{ref} is the reference area, v is the velocity of the incident atmospheric particles, hence the orbiting velocity, ρ is the free-stream density that varies with the altitude, and c_d is the drag coefficient. Since A_{ref} is a fixed geometrical parameter, v depends on the orbit type, and ρ is defined when the altitude is selected, the only source of uncertainty for the drag estimation is the c_d. The three main strategies for estimating the c_d are assigning a fixed value, calculating it by semi-empirical models, or determining it with physical models and simulations. The DSMC simulations can directly calculate the value of D without assigning the c_d a priori. Thus, as a final remark of this study, the different drag forces for case 1 and case 8 are calculated with the DSMC simulations. Before comparing the drag force values of cases 1 and 8, this study's numerical framework is validated against the literature case. The reference case for the validation is the slope geometry [18] a fully diffuse reflection (α_{acc}=1.0). For this case, the drag resulting from the DSMC simulation from this study is $\sim$ 34.2 mN, with a 1.15% error if compared to the reference case from literature [18] (34.5983 mN). Moving on to this study's partially diffuse reflection ($\alpha_{acc} = 0.55$) cases, for the Earth case at 180 km (case 1), the drag is $\sim$29.7 mN, whereas for case 8 in Mars orbit at 140 km altitude, the drag is $\sim$12.5 mN. Hence, the drag from case 8 is $\sim$42% of the one for Earth in case 1. Since A_{ref} is the same, an additional qualitative check on the DSMC results can be derived by comparing the differences in the DSMC results by the the product $\rho \cdot v^2$: for case 1 is 31.303 N m^{-2}, for case 8 is 12.72 N m^{-2}, hence it is $\sim$40.6% of case 1, which is reasonable in agreement with the $\sim$42% from the simulations. Additionally, the drag coefficient c_d for case 1 and case 8 can be estimated. Considering the reference area as the frontal area of $\sim$1.77 m^2 calculated with the external radius of 0.75 m for the investigated geometry from the literature [18], the c_d is $\sim$1.07 and $\sim$1.11 for case 1 and case 8 respectively with partially diffuse GSI, whereas for case 1 with completely diffuse reflection ($D = \sim$ 34.2 mN) the c_d is $\sim$1.23.

Conclusions

Ground tests and numerical simulations can provide a synergic approach to tackle the design of ABEP for planetary and orbit-specific missions, leading to reliable prototypes for future in-orbit demonstrations. At the beginning of this study, the atmospheric

characterization is achieved by collecting and comparing data from several missions and models for both Earth and Mars. These data are key parameters for establishing the functioning of the ABEP systems. The presented DSMC-based numerical framework aims to characterize the collection and compression performances and to estimate the drag force. A test case with a simplified geometry from the literature is taken as a reference for the simulation of low orbits of both Earth and Mars. The tests of the DSMC-based numerical framework focus on the impact of GSI models (specular, total and partially diffuse, and lobular reflection) with a brief check on the influence of the interparticle collision models (VHS and VSS). Slight differences are observed between VHS (case 1) and VSS (case 3), as well as the inclusion of gas-phase reactions (case 2). As for the GSI model, the specular reflection (case 4) results in higher compression performance, whereas the Maxwellian model (case 1) yields similar results to the CLL with an anisotropic scattering kernel (case 7), whereas different values stem from the case with the isotropic kernel (case 6). Finally, the comparison between two Martian low-orbits cases and the Earth case at 180 km is presented. With the Maxwellian partially diffuse reflection, the case at 140 km (case 8) is comparable to case 1 in terms of number density values, including in the proximity of the ionization stage inlet. However, the maximum pressure increase along the axisymmetry line is 49% less than case 1 (Earth 180 km), but the aerodynamic drag force calculated by the DSMC method is 39% less for case 8 if compared to case 1. After this comparison between Mars and Earth's low orbit performance, further development in design optimization could be the next required step. This study provides an extensive comparison of the results that stem from different modelling strategies, offering an advantageous starting point for the geometry design. Moreover, the validated numerical framework can be easily reproduced and employed for the ABEP intake optimization to ensure an adequate mass flow rate for the electric thruster. Finally, the comparison between the Earth and Mars applications aims at a preliminary investigation of the use of this technology for other target planets.

Nomenclature

ABEP	Atmosphere Breathing Electric Propulsion
AETHER	Air-breathing Electric THrustER
CLL	Cercignani Lampis Lord
DSMC	Direct Simulation Monte Carlo
GSI	Gas-surface Interaction
LEO	Low Earth Orbit
MABHET	Martian Atmosphere Breathing Hall Effect Thruster
MAVEN	Mars Atmosphere and Volatile EvolutioN
NGISM	Neutral Gas ans Ion Mass Spectrometer
RPA	Retarding Potential Analyzer
S/C	Space Craft
SPARTA	Stochastic PArallel Rarefied-gas Time-accurate Analyzer
TCE	Total Collision Energy
UAMS	Upper Atmosphere Mass Spectrometer

VHS	Variable Hard Sphere
VLEO	Very Low Earth Orbit
VSS	Variable Soft Sphere
A_{ioniz}	area of the cross section of the ionization stage
A_{ref}	reference area for aerodynamic drag
c_d	drag coefficient
D	atmospheric drag force
d_{ref}	reference diameter for particle collision
E_i	kinetic energy of the incident particle
E_r	energy of the re-emitted particle
E_w	energy the particle needs to deplete to reach thermal equilibrium with the wall
h	altitude
$\mathrm{k_B}$	Boltzmann constant
Kn	Knudsen number
L_c	characteristic length for the Knudsen number
L_{cell}	computation grid cell dimension
m_p	mass of the particles
MW_{ave}	average molecular weight of atmospheric mixture at a given altitude
n	number density
n_{tot}	total number density
N_A	Avogadro number
p	pressure
R	ideal gas constant
r_{ref}	reference diameter of the ionization stage
s	speed ratio
x_i	mole fraction of species i
v	velocity
v_b	bulk velocity
v_{orb}	orbiting velocity of the satellite
$v_{thermal}$	thermal velocity
α	exponent of the VSS and VHS molecular models
α_{acc}	accommodation coefficient
$\alpha_{acc,n}$	accommodation coeff. in the normal direction
$\alpha_{acc,rot}$	accommodation coeff. for the rotational energy
$\alpha_{acc,t}$	accommodation coeff. in the tangential direction
$\alpha_{acc,vib}$	accommodation coeff. for the vibrational energy
λ	molecular mean free path
ρ	mass density
ω	temperature exponent in the viscosity calculation for the molecular models

Acknowledgements
A special thanks to Aloha Mingo and Pavel Smirnov for the fruitful discussions regarding the development of the atmosphere-breathing electric propulsion systems. This project is part of the SeRANIS project (dtec.unibw). Computational resources (HPC cluster HSUper) have been provided by the project hpc.bw, funded by dtec.bw - Digitalization

and Technology Research Center of the Bundeswehr. dtec.bw is funded by the European Union - NextGenerationEU. We acknowledge financial support by Universität der Bundeswehr München.

Funding
Open Access funding enabled and organized by Projekt DEAL. No funding was received for conducting this study.

Data availability
No datasets were generated or analysed during the current study.

Declarations

Competing interests
The authors declare no competing interests.

Received: 22 August 2024 Accepted: 4 November 2024
Published online: 20 November 2024

References

1. Filatyev A, Golikov A, Erofeev A, Khartov S, Lovtsov A, Padalitsa D, Skvortsov V, Yanova O (2023) Research and development of aerospace vehicles with air breathing electric propulsion: Yesterday, today, and tomorrow. Prog Aerosp Sci 136:100877
2. Andreussi T, Ferrato E, Giannetti V (2022) A review of air-breathing electric propulsion: from mission studies to technology verification. J Electr Propuls 1(1):31
3. Zheng P, Wu J, Zhang Y, Wu B (2020) A comprehensive review of atmosphere-breathing electric propulsion systems. Int J Aerosp Eng 2020:1–21
4. Hohman K (2012) Atmospheric breathing electric thruster for planetary exploration. 11:1–35
5. Di Cara D, Del Amo JG, Santovincenzo A, Dominguez BC, Arcioni M, Caldwell A, Roma I (2007) Ram electric propulsion for low earth orbit operation: an esa study, vol 21. 30th IEPC - International Electric Propulsion Conference, Florence, p 22
6. Nishiyama K (2003) Air breathing ion engine concept. In: 54th International Astronautical Congress of the International Astronautical Federation, the International Academy of Astronautics, and the International Institute of Space Law, American Institute of Aeronautics and Astronautics. https://doi.org/10.2514/6.IAC-03-S.4.02
7. Tagawa M, Yokota K, Nishiyama K, Kuninaka H, Yoshizawa Y, Yamamoto D, Tsuboi T (2013) Experimental study of air breathing ion engine using laser detonation beam source. J Propuls Power 29(3):501–506
8. Andreussi T, Ferrato E, Paissoni C, Kitaeva A, Giannetti V, Piragino A, Schäff S, Katsonis K, Berenguer C, Kovacova Z et al (2022) The aether project: development of air-breathing electric propulsion for vleo missions. CEAS Space J 14(4):717–740
9. Romano F, Binder T, Herdrich G, Fasoulas S, Schönherr T (2016) Intake design for an atmosphere-breathing electric propulsion system. Space Propuls 1–11
10. Romano F, Chan YA, Herdrich G, Traub C, Fasoulas S, Roberts P, Smith K, Edmondson S, Haigh S, Crisp N et al (2020) Rf helicon-based inductive plasma thruster (ipt) design for an atmosphere-breathing electric propulsion system (abep). Acta Astronaut 176:476–483
11. Romano F, Espinosa-Orozco J, Pfeiffer M, Herdrich G, Crisp NH, Roberts P, Holmes B, Edmondson S, Haigh S, Livadiotti S et al (2021) Intake design for an atmosphere-breathing electric propulsion system (abep). Acta Astronaut 187:225–235
12. Crisp NH, Roberts PC, Livadiotti S, Oiko VTA, Edmondson S, Haigh S, Huyton C, Sinpetru L, Smith K, Worrall S et al (2020) The benefits of very low earth orbit for earth observation missions. Prog Aerosp Sci 117:100619
13. Wu L (2022) Rarefied gas dynamics: kinetic modeling and multi-scale simulation. Springer Nature, Singapore. https://doi.org/10.1007/978-981-19-2872-7
14. Bird GA (1994) Molecular gas dynamics and the direct simulation of gas flows. Oxford University Press, Oxford
15. Fasoulas S, Munz CD, Pfeiffer M, Beyer J, Binder T, Copplestone S, Mirza A, Nizenkov P, Ortwein P, Reschke W (2019) Combining particle-in-cell and direct simulation monte carlo for the simulation of reactive plasma flows. Phys Fluids 31(7):072006. https://doi.org/10.1063/1.5097638
16. Rapisarda C, Roberts PC, Smith KL (2023) Design and optimisation of a passive atmosphere-breathing electric propulsion (abep) intake. Acta Astronaut 202:77–93
17. Jin X, Cheng X, Huang Y, Wang Q, Wang B, Shen Q (2023) Numerical analysis of inlet flows at different altitudes in the upper atmosphere. Phys Fluids 35(9):09365. https://doi.org/10.1063/5.0160002
18. Jin X, Miao W, Cheng X, Wang Q, Wang B (2024) Monte Carlo simulation of inlet flows in atmosphere-breathing electric propulsion. AIAA J 62(2):518–529
19. Zheng P, Wu J, Zhang Y et al (2021) Design and numerical investigation on the intake of atmosphere-breathing electric propulsion. Acta Astronaut 188:215–228
20. Maxwell JC (1879) Vii. on stresses in rarified gases arising from inequalities of temperature. Philos Trans R Soc Lond 170:231–256
21. Cercignani C, Lampis M (1971) Kinetic models for gas-surface interactions. Transp Theory Stat Phys 1(2):101–114
22. Lord R (1991) Some extensions to the cercignani-lampis gas-surface scattering kernel. Phys Fluids A Fluid Dyn 3(4):706–710

23. Picone JM, Hedin AE, Drob DP, Aikin AC (2002) Nrlmsise-00 empirical model of the atmosphere: Statistical comparisons and scientific issues. J Geophys Res Space Phys 107(A12):SIA 15–1–SIA 15–16. https://doi.org/10.1029/2002JA009430
24. Crandall P, Wirz RE (2022) Air-breathing electric propulsion: mission characterization and design analysis. J Electr Propuls 1(1):12
25. Emmert JT, Drob DP, Picone JM, Siskind DE, Jones Jr M, Mlynczak MG, Bernath PF, Chu X, Doornbos E, Funke B, Goncharenko LP, Hervig ME, Schwartz MJ, Sheese PE, Vargas F, Williams BP, Yuan T (2021) Nrlmsis 2.0: A whole-atmosphere empirical model of temperature and neutral species densities. Earth Space Sci 8(3):e2020EA001321. https://doi.org/10.1029/2020EA001321
26. Seiff A, Kirk DB (1977) Structure of the atmosphere of mars in summer at mid-latitudes. J Geophys Res 82(28):4364–4378
27. Haider S, Mahajan K (2014) Lower and upper ionosphere of mars. Space Sci Rev 182(1):19–84
28. Blanchard RC, Wilmoth RG, Moss JN (1997) Aerodynamic flight measurements and rarefied-flow simulations of mars entry vehicles. J Spacecr Rocket 34(5):687–690
29. Justus C, James B, Bougher S, Bridger A, Haberle R, Murphy J, Engel S (2002) Mars-gram 2000: A mars atmospheric model for engineering applications. Adv Space Res 29(2):193–202
30. Schofield J, Barnes JR, Crisp D, Haberle RM, Larsen S, Magalhaes J, Murphy JR, Seiff A, Wilson G (1997) The mars pathfinder atmospheric structure investigation/meteorology (asi/met) experiment. Science 278(5344):1752–1758
31. Barth CA, Stewart A, Hord C, Lane A (1972) Mariner 9 ultraviolet spectrometer experiment: Mars airglow spectroscopy and variations in lyman alpha. Icarus 17(2):457–468
32. Barth CA (1974) The atmosphere of mars. Ann Rev Earth Planet Sci 2(1):333–367
33. O'Nier A, McElroy MB (1977) Composition and structure of mars' upper atmosphere: Results from the neutral mass spectrometers on viking 1 and 2. J Geophys Res 82(28):4341–4349
34. Mahaffy PR, Benna M, Elrod M, Yelle RV, Bougher SW, Stone SW, Jakosky BM (2015) Structure and composition of the neutral upper atmosphere of mars from the maven ngims investigation. Geophys Res Lett 42(21):8951–8957
35. Lillis RJ, Brain DA, Bougher SW, Leblanc F, Luhmann JG, Jakosky BM, Modolo R, Fox J, Deighan J, Fang X et al (2015) Characterizing atmospheric escape from mars today and through time, with maven. Space Sci Rev 195:357–422
36. Plimpton S, Moore S, Borner A, Stagg A, Koehler T, Torczynski J, Gallis M (2019) Direct simulation monte carlo on petaflop supercomputers and beyond. Phys Fluids 31(8):086101. https://doi.org/10.1063/1.5108534
37. Pfeiffer M (2022) An optimized collision-averaged variable soft sphere parameter set for air, carbon, and corresponding ionized species. Phys Fluids 34(11):117110. https://doi.org/10.1063/5.0118040
38. Park C, Howe J, Jaffe R, Candler G (1991) Chemical-kinetic problems of future nasa missions. AIAA Meeting Papers, 29th Aerospace Sciences Meeting, Reno, NV, p 464
39. Moe K, Moe MM (2005) Gas-surface interactions and satellite drag coefficients. Planet Space Sci 53(8):793–801
40. Mehta PM, Linares R, Sutton EK (2019) Data-driven inference of thermosphere composition during solar minimum conditions. Space Weather 17(9):1364–1379. https://doi.org/10.1029/2019SW002264

Publisher's Note